Journal of
Composites Science

MDPI

Article

Determination of Fatigue Damage Initiation in Short Fiber-Reinforced Thermoplastic through Acoustic Emission Analysis

Janna Krummenacker * and Joachim Hausmann

Department of Fatigue and Life Time Prediction, Leibniz-Insitut für Verbundwerkstoffe GmbH, 67663 Kaiserslautern, Germany; joachim.hausmann@ivw.uni-kl.de
* Correspondence: janna.krummenacker@ivw.uni-kl.de

Abstract: This study investigates the damage initiation in short glass fiber-reinforced polyamide 6.6 under fatigue loading using acoustic emission analysis. An optimized specimen geometry was developed to meet the specific requirements of this testing method, at the same time allowing further micromechanical studies. Specimens were preloaded with tensile–tensile fatigue loading, varying the maximum stress and the number of load cycles. Subsequently, the acoustic emission signals in residual strength tests were compared to those of undamaged specimens. The idea behind this approach is that only the damage that has not already occurred under fatigue load can be recorded in the residual strength tests. Using the analysis of acoustic energy, a stress threshold for damage initiation was identified. Furthermore, with tension–tension fatigue tests, the SN curve of the material was determined to estimate the lifetime for the identified stress threshold. The presented approach allows us to estimate a so-called endurance limit of short glass fiber-reinforced polyamide 6.6.

Keywords: fatigue; damage initiation; thermoplastic; short glass fiber reinforced thermoplastics; acoustic emission

Citation: Krummenacker, J.; Hausmann, J. Determination of Fatigue Damage Initiation in Short Fiber-Reinforced Thermoplastic through Acoustic Emission Analysis. *J. Compos. Sci.* **2021**, *5*, 221. http://doi.org/10.3390/jcs5080221

Academic Editor: Francesco Tornabene

Received: 9 July 2021
Accepted: 16 August 2021
Published: 19 August 2021

1. Introduction

Short glass fiber-reinforced thermoplastics (SFRT) are increasingly used in technical components thanks to their good mechanical properties and their flexible moldability. While their use was often limited to housings in the past, they are now also becoming more and more common in load-bearing components. Their mechanical properties are highly anisotropic due to the fiber orientation distribution, resulting from the injection molding process [1,2]. Therefore, micromechanical modeling of SFRT remains challenging. Homogenization approaches using transverse isotropic material models have been shown to be suitable for this task [3–5]. The Tsai–Hill criterion predicted the failure of SFRT with good agreement with experimental data [6–8].

Additionally, SFRT are highly sensitive to humidity and temperature due to the thermoplastic matrix, i.e., polyamide [9,10]. Therefore, a complete mechanical characterization of the material requires great experimental effort, especially for fatigue tests. Given that SFRT behaves with high sensitivity to temperature changes, the fatigue testing frequency has to be limited in such a manner that the temperature rise stays within defined limits [11]. With the mechanical properties depending on various factors and the fact that fatigue testing itself is very time consuming, a complete material characterization of SFRT under fatigue loading is very expensive.

Therefore, the presented research aims to develop a time-efficient test method that allows us to draw conclusions about the damage behavior under fatigue loading. Acoustic emission (AE) is a popular tool to gain information on the micro-structural damage mechanisms under mechanical loading. However, most of the studies published so far focused on continuous fiber-reinforced plastics [12–19]. Sato et al. [20] performed the first

experiments with AE on SFRT in the 1980s. In these tests, crack initiation and crack growth in the interface as well as in the matrix were distinguished based on the amplitude of the captured acoustic signals. Schoßig et al. [21] used the amplitude and energy of AE signals to discriminate the damage mechanisms in tensile tests of SFRT. Another common approach is to examine the frequency features of the acoustic signals in order to assign them to different damage mechanisms [22].

Due to the high amount of data, AE is mostly used in quasi-static tests, and is not suitable for the use in fatigue tests itself. This is why Bauer et al. [23] used the frequency features of acoustic signals in quasi-static tensile tests to relate them to the fatigue behavior of SFRT. Another difficulty using AE in fatigue tests is the high exposure to background noise, since fatigue tests are often performed on servo-hydraulic testing machines [24]. To the authors' knowledge, Williams et al. [25] were the first to overcome these challenges, recording AE data during fatigue tests for about 1.5 million cycles. In this way, they were able to establish a correlation between AE and damage to continuous fiber-reinforced composite specimens. Schorer et al. [26] studied damage progression in low-cycle fatigue tests using acoustic emission analysis. The recording of acoustic emission data during fatigue tests remains a challenging task, especially for tests in the high cycle or even very high cycle regime.

To overcome the difficulties mentioned above, the following study investigates correlations between the material behavior under static and under fatigue loading. For this purpose, some of the test specimens were subjected to cyclic preloading, while the rest stayed unloaded. Subsequently, quasi-static tensile tests combined with AE testing were performed. For the unloaded specimens, the AE captured the damage introduced by quasi-static tensile loading. For the preloaded specimens, these tests corresponded to residual strength tests, where the AE only captured the damage that had not yet been completed during the cyclic preloading. By comparing the AE data of unloaded and preloaded specimens, the damage state of the preloaded specimens could be evaluated.

2. Materials and Methods

The material under investigation was a short fiber-reinforced polyamide 6.6 containing 40 wt.% glass fibers (Lehmann&Voss&Co. KG, Hamburg, Germany). Plates with a thickness of 3 mm were produced in the injection molding process, from which the test specimens were subsequently extracted by milling in the direction of injection molding.

Future work will compare experimental results with a digital twin. This led to specific requirements for the specimen geometry. To resolve a single fiber with multiple voxels, the resolution of the X-ray scan had to be less than 3.0 µm. This resulted in a limitation of the dimensions of the gauge cross-section to a maximum of 8×8 mm^2. To model the gauge cross-section with reasonable computational effort, the width was reduced to the thickness of a plate, resulting in a square cross-section of 3×3 mm^2. In order for the microphones with a diameter of 8 mm to fit completely on the specimen, the width of the measuring length had to increase.

The optimization of the specimen geometry was performed with the software LS-OPT® from DYNAmore. During the optimization process, the stresses were determined using the finite element analysis software Abaqus®. Figure 1a shows the optimized specimen geometry, in which the expansion from the gauge section to the cross-section where the sensors are mounted was realized with a spline. The sensors were applied as symmetrically as possible, within a distance of approx. 38.0 mm from each other. Figure 1b shows an image of an X-ray scan of the gauge length with a resolution of 2.0 µm. The typical core shell morphology can be observed, where the fibers in the shell layers are mainly oriented in the direction of injection molding. Using the coordinate system depicted in Figure 1, the averaged fiber orientation tensor of the analyzed volume was calculated using classical imaging techniques as:

$$a = \begin{bmatrix} 0.544 & 0 & 0.001 \\ - & 0.370 & -0.003 \\ - & - & 0.086 \end{bmatrix} \quad (1)$$

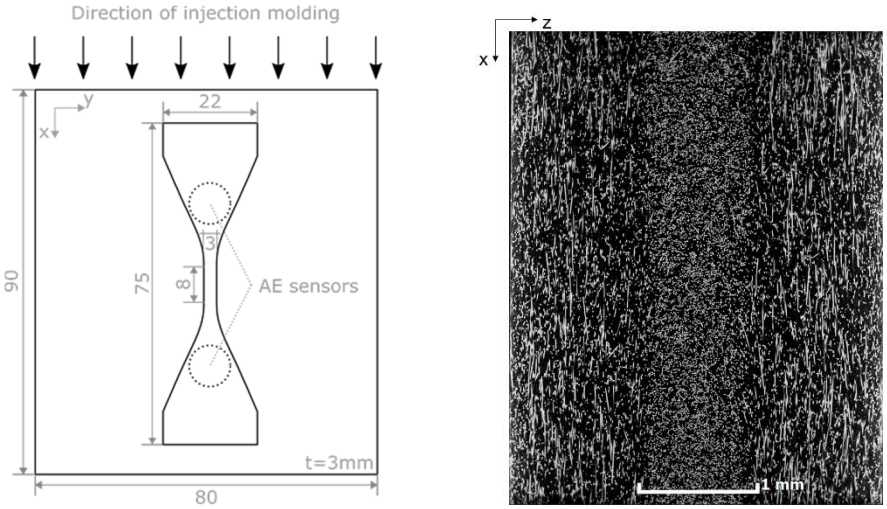

Figure 1. (**a**) Optimized specimen geometry with schematic position of AE sensors, dimensions in mm; (**b**) exemplary cross section within the gauge length resolved from an X-ray scan with a resolution of 2.0 µm. Direction of injection molding is along the *x*-axis.

The fiber orientation tensor shows that the fibers are mainly oriented in and transverse to the direction of injection molding. This is why a transverse isotropic material law from previous studies was used in the optimization process [27]. The Tsai–Hill failure criterion was used to calculate the material effort by means of a user subroutine. The objective of the optimization process was to provoke a failure due to microstructural stress concentrations instead of stress concentrations resulting of the specimen geometry. This was implemented in such a way that the ratio between the maximum stress and the average stress within the gauge length was minimized. Therefore, the parameters of a quadratic Bézier curve were optimized for a smooth transition from the narrow to the wide cross section.

Part of the specimens were cyclically preloaded on an electrodynamic testing machine (ElectroForce 3550, TA Instruments, New Castle, DE, USA). The testing was conducted under load control in tension–tension mode with a constant load ratio R = 0.1 and a testing frequency of 10 Hz at room temperature (23 °C and 40% relative humidity). An infrared camera (PI400, Optris, Berlin, Germany) randomly monitored the temperature of the specimen surface and showed that the temperature rise due to the cyclic loading was limited to 3 K.

In the first series of tests, 10 specimens were preloaded with 10^5 load cycles at different maximum stress levels. The stress levels were chosen between 20.0 and 79.8 MPa, which corresponds to 13% and 53% of the quasi-static strength. In the second series of tests, five specimens were preloaded with the same maximum stress level of 59.9 MPa (40% of the quasi-static strength) up to a number of load cycles ranging between 10^2 and 10^7. Table 1 shows the test matrix for the preloading of the specimens.

Table 1. Test matrix of fatigue preloading.

Maximum Stress in MPa	Relative Maximum Stress	Number of Cycles					
		10^2	10^3	10^4	10^5	10^6	10^7
79.8	0.53				x		
73.2	0.48				x		
66.5	0.44				x		
59.9	0.40	x	x	x	x	x	x
53.2	0.35				x		
46.6	0.31				x		
39.9	0.26				x		
33.3	0.22				x		
26.6	0.18				x		
20.0	0.13				x		

The tests for the SN curve were performed under the same conditions as the preloading tests. Nineteen specimens were tested until either rupture or, in the case of no failure, stopped after 10^7 cycles and marked as run-outs. In order to capture the behavior in the low cycle regime as well as in the high cycle regime, the tests were carried out with different maximum stresses between 59.9 and 86.5 MPa.

The quasi-static tests were run on a mechanical testing machine (RetroLine, Zwick-Roell, Ulm, Germany) at room temperature under displacement control. According to DIN EN ISO 527-1 [28], the speed of movement of the machine crosshead was 1 mm/min and the force was measured with a 10 kN load cell. Pneumatic jaws at a distance of 60 mm clamped the specimens. Within the gauge length, the strain was measured by means of digital image correlation (DIC) using the camera system Aramis4M (gom) with a recording frequency of five frames per second.

Two acoustic sensors (AE104A, Vallen Systeme GmbH, Wolfratshausen, Germany) were placed approx. 12 mm from the clamping (Figure 2). A silicon grease was used to create coupling between the sensors and the specimen surface. Prior to each test, the exact distance of the sensors was determined by three pencil lead breaks at the height of each sensor. In this way, it was possible to localize the acoustic events during the test and filter those events that occurred outside the gauge section. The signals were recorded with the system AMSY−5 (Vallen Systeme GmbH, Wolfratshausen, Germany) and with the use of two preamplifiers (AEP4, Vallen Systeme GmbH, Wolfratshausen, Germany) with the gain set to 40 dB. As soon as the threshold defined at 2.52×10^{-5} mV (corresponds to 28 dB) was exceeded, the respective sensor started to store the data with a sample rate of 10 MHz. The total length of a hit was recorded with 4096 samples, corresponding to a hit duration of 409.6 µs. A so-called pre-trigger, i.e., the data before the registered threshold crossing, was set to 512 samples.

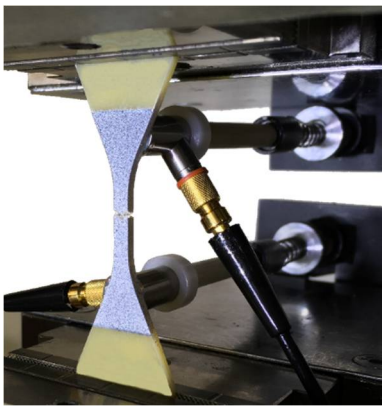

Figure 2. Test set-up: broken specimen with acoustic sensors and speckle pattern for DIC.

A custom python script was used to analyze the acoustic data. To shorten the runtime, the filtering of the data was performed in three steps. The first step was to filter out the events that did not occur within the distance between the two sensors. For the remaining events, the hit arrival times defined by the first threshold crossing were adjusted with the help of the Akaike information criterion (AIC) [29]. Subsequently, the origin of the damage event was calculated based on the corrected arriving times using a sound velocity of 3274 m/s. This velocity had been previously determined for the plates in the injection molding direction with a standard deviation of ±125 m/s. Based on the localization, the second stage of filtering was performed by filtering out the events that did not occur within the measurement length. In a final step, the events were divided into the first and second hits. Only the first hits were included in the further analysis, i.e., the acoustic signals recorded by the sensor that was closer to the damage event.

3. Results and Discussion

3.1. Preloading with Different Maximum Stresses

A typical acoustic energy distribution and accumulated acoustic energy evolution of a non-preloaded specimen during the tensile test as well as the stress–strain curve are plotted in Figure 3. It can be observed that the acoustic hits are first captured at a strain value of approx. 0.5%. It is also noted that the maximum acoustic energy increases with increasing stress. Up to a strain of approx. 3%, numerous events with an acoustic energy below 10^3 e.u. occur. After that, these events occur only sporadically, and the acoustic energy of most sound events is above 10^3 e.u.

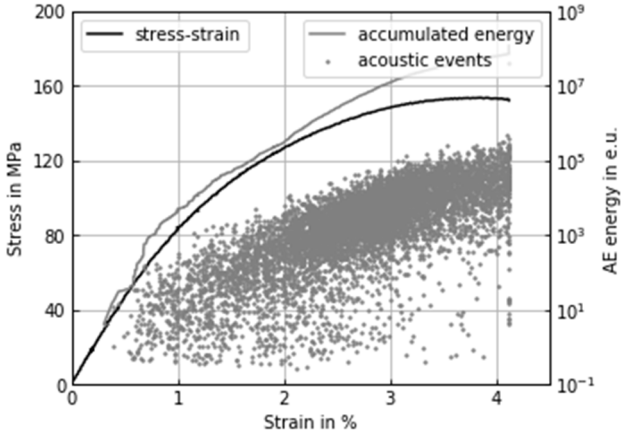

Figure 3. Stress–strain curve, acoustic energy and accumulated acoustic energy in energy units (1 e.u. $\hat{=}$ 1×10^{-21} J) of unloaded specimen.

Figure 4 shows the stress–strain curves, the acoustic energy distribution and accumulated acoustic energy evolution of four specimens preloaded with 10^5 load cycles, each with a different maximum stress level. A comparison of Figures 3 and 4 shows that the point clouds of the preloaded specimens differ significantly from those of the unloaded specimens. For the preloaded specimens, the first acoustic hits occur at a strain slightly higher than the strain applied during preloading. Accordingly, the stress at the start of the acoustic activity and thus during the damage events exceeds the applied maximum stress of the fatigue loading. This means that in the residual strength tests, the damage events only start at a strain that is higher than the strain applied during cyclic preloading. This observation leads to the conclusion that during constant deformation, cyclic loading causes more damage than quasi-static loading.

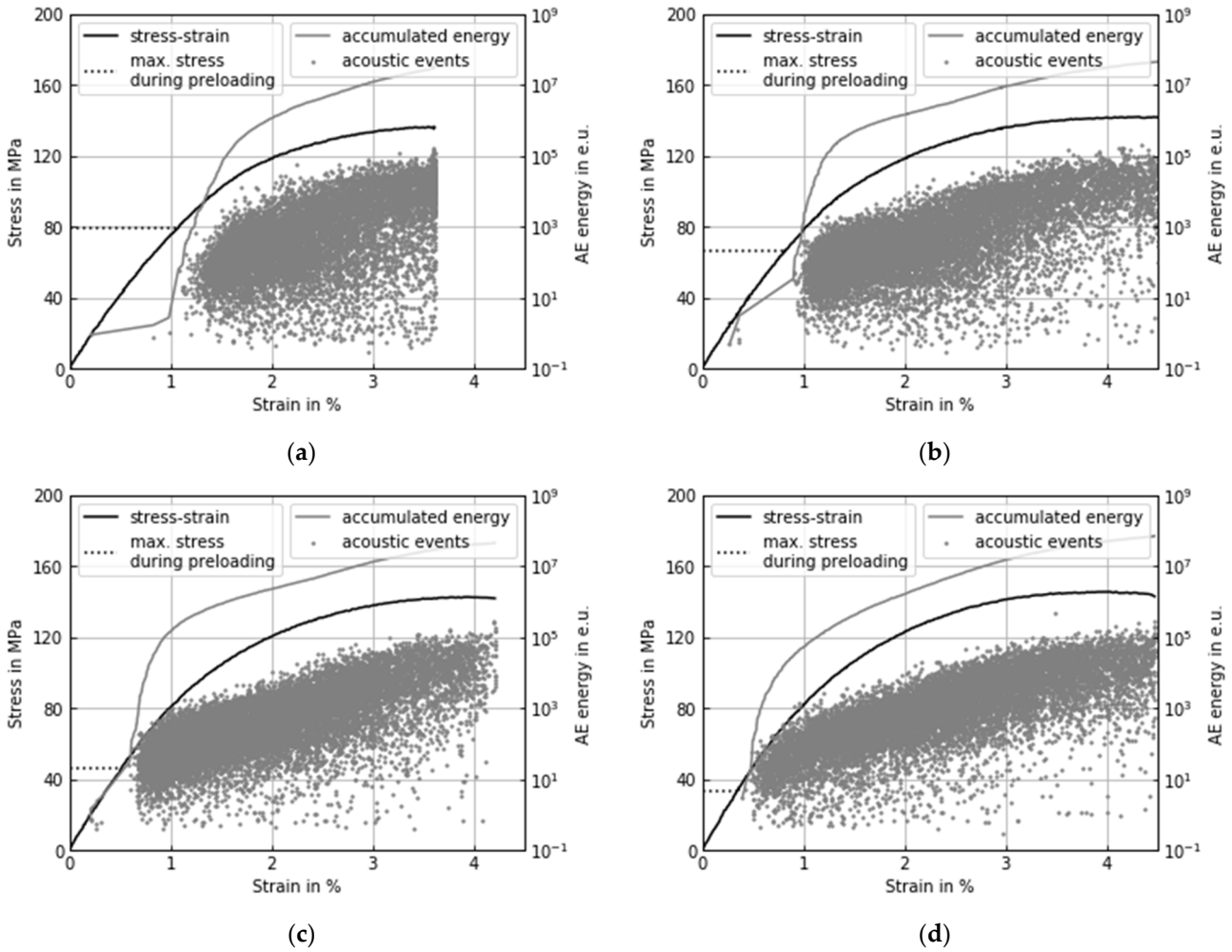

Figure 4. Stress–strain curve, acoustic energy and accumulated acoustic energy in energy units (1 e.u. $\hat{=}$ 1×10^{-21} J) of preloaded specimens: σ_{max} = (**a**) 79.8 MPa; (**b**) 66.5 MPa; (**c**) 46.6 MPa; (**d**) 33.3 MPa.

Figure 4 also shows that the point cloud is already very dense at the onset, and the curve of the accumulated acoustic energy is very steep in the beginning. Accordingly, the damage events in the tests with the preloaded specimens start very promptly after exceeding a certain strain. The unloaded specimen, on the other hand, shows a different behavior. A typical damage process can explain this observation: at low deformation levels, the first micro-cracks develop at the highest stress concentrations. These stress concentrations can occur at fiber ends or where fibers are very close to each other. Crack initiation is thus a stochastically distributed process that does not appear suddenly. In a second step, these micro-cracks continue to grow as soon as the deformation work is large enough. With cyclic preloading, the first part of the damage, the crack initiation, is largely completed. Therefore, in the residual strength tests, only acoustic events resulting from crack growth of the already existing micro-cracks are registered. These micro-cracks continue to grow as soon as the deformation work is sufficiently high.

Figure 5 shows the results of the two specimens preloaded with the smallest stresses in this series of tests. The point clouds and the accumulated energy curves are similar to those of the unloaded specimen in Figure 3 and different from the point clouds and the accumulated energy curves of the specimens preloaded with higher stresses in Figure 4. The authors interpret this as a sign that the cyclic preloading did not initiate damage.

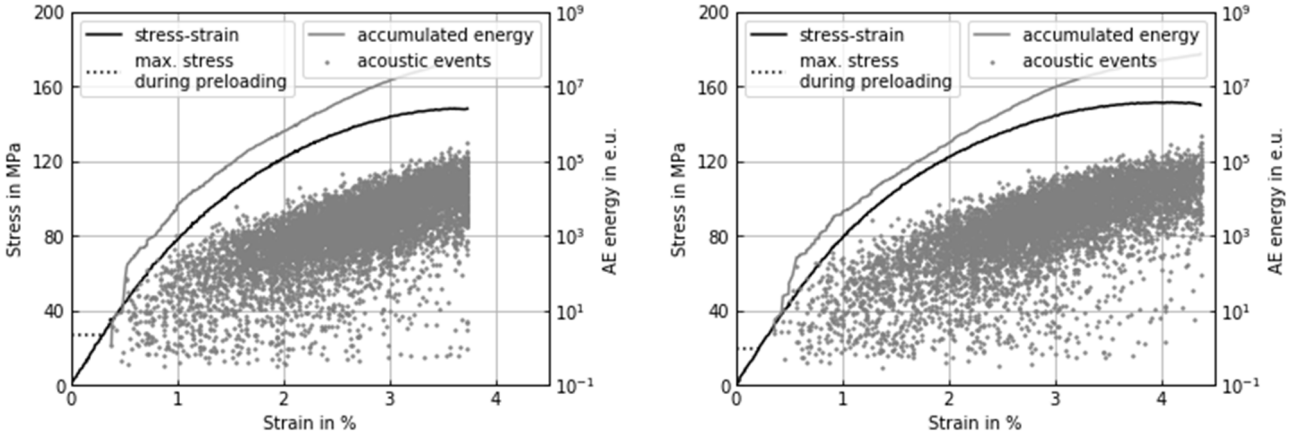

Figure 5. Stress–strain curve, acoustic energy and accumulated acoustic energy in energy units (1 e.u. $\hat{=}$ 1×10^{-21} J) of preloaded specimens: σ_{max} = (**a**) 26.6 MPa; (**b**) 20.0 MPa.

Figure 6 shows the accumulated acoustic energy curves of the unloaded and the preloaded specimens to summarize the above presented reflections. The characteristic of the curves of the preloaded specimens changes from a maximum stress below 40 MPa and approaches the curves of the unloaded specimens. This observation suggests that the state of damage initiation at this stress level was not yet fully completed by the cyclic preloading. This implies that the damage behavior changes below this stress level. If the maximum stress during preloading is less than 26.6 MPa, the accumulated acoustic energy behaves similarly to that of the unloaded specimens. This means that the applied cyclic preload did not cause any measurable damage.

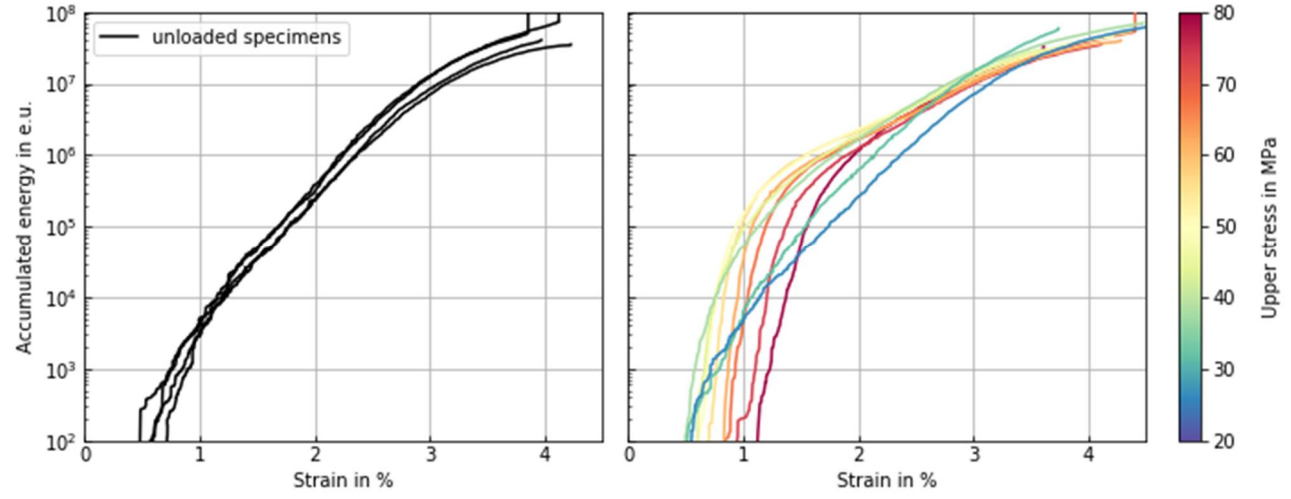

Figure 6. Accumulated acoustic energy in energy units (1 e.u. $\hat{=}$ 1×10^{-21} J): (**a**) unloaded specimens; (**b**) preloaded specimens sorted by upper stress level.

3.2. Preloading with Different Number of Cycles

In this section, the influence of the number of cycles on the damage state is studied. Figure 7 shows the stress–strain curve, the acoustic events, and the accumulated acoustic energy of the specimens preloaded with the same maximum stress but with a different number of cycles. The number of cycles and thus the damage state decreases from upper

left to the lower right. It is noticeable that with a preloading of 10^4 and 10^3 cycles, a few hundred acoustic hits occur very early or at low strain. After these first acoustic events, there is a pause until the next events occur at a strain of about 0.8%. This observation is also consistent with the assumptions about damage process explained above. In the first part of the lifetime, micro-cracks are initiated up to a certain number of load cycles. A phase of stable crack growth is subsequently established. At a maximum stress of 59.9 MPa, this stage of stable crack growth is reached only after a service life of 10^5 load cycles. Before these 10^5 load cycles are completed, further micro-cracks are induced that require little additional deformation work in the residual strength tests to grow. The plot of the specimen preloaded only with 10^2 load cycles also differs from all others and resembles the curve of an unloaded specimen (see Figure 3). This suggests that the first 10^2 load cycles cause too little damage to be noticeable in the residual strength tests.

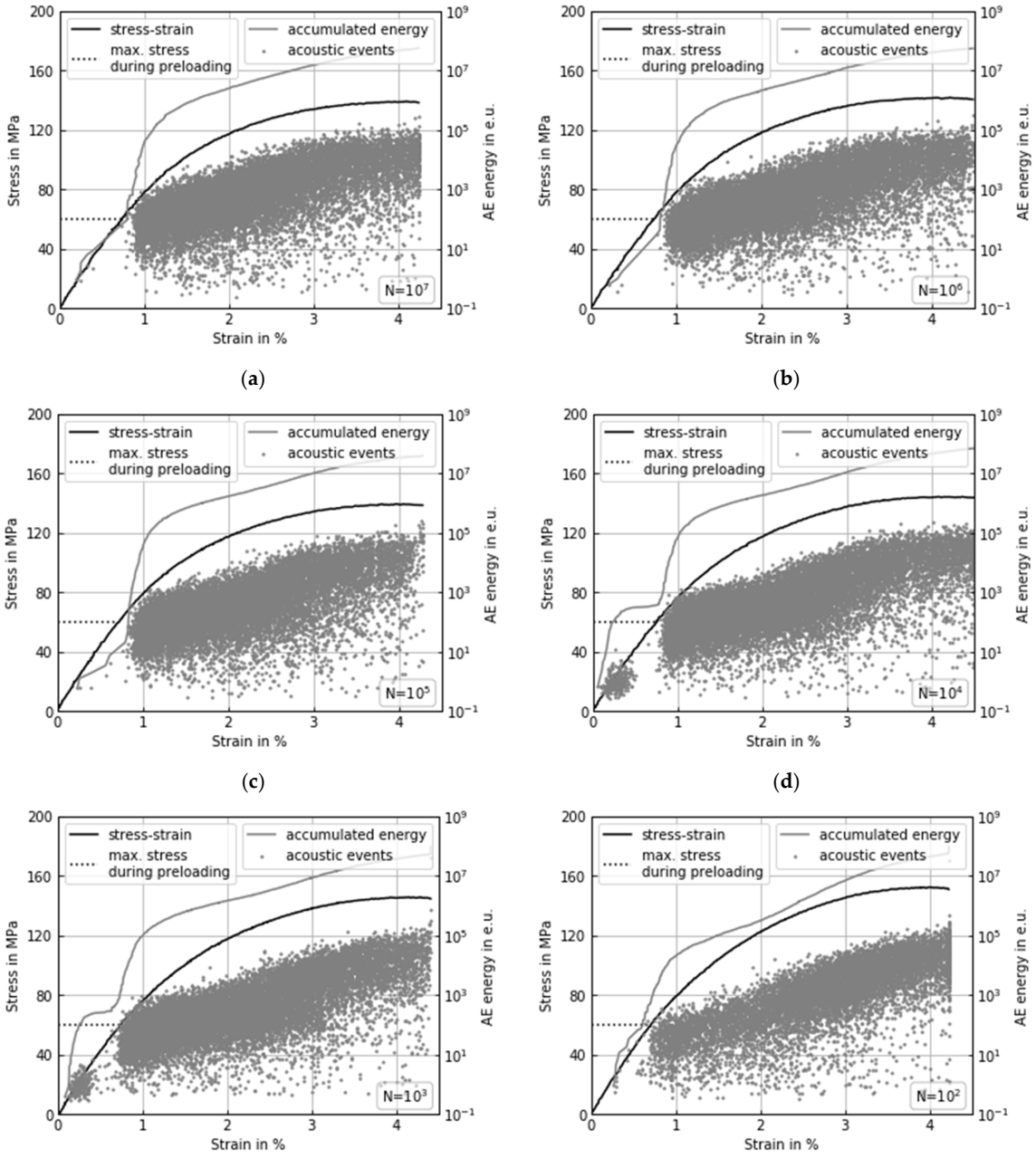

Figure 7. Stress–strain curve, acoustic energy and accumulated acoustic energy in energy units (1 e.u. $\hat{=}$ 1×10^{-21} J) of preloaded specimens with σ_{max} = 59.9 MPa: (**a**) 10^7; (**b**) 10^6; (**c**) 10^5; (**d**) 10^4; (**e**) 10^3; (**f**) 10^2 cycles.

Figure 8 summarizes the accumulated acoustic energy curves for the undamaged specimens and the specimens that were preloaded with a different number of load cycles. All curves of the preloaded specimens differ from the curves of the unloaded specimens. The curve of the specimen preloaded with 10^2 load cycles is flatter than the other curves. For a preloading with 10^3 and 10^4 load cycles, a few hits occur at a low strain. The three specimens preloaded with 10^5, 10^6 and 10^7 load cycles show the same trend of accumulated acoustic energy.

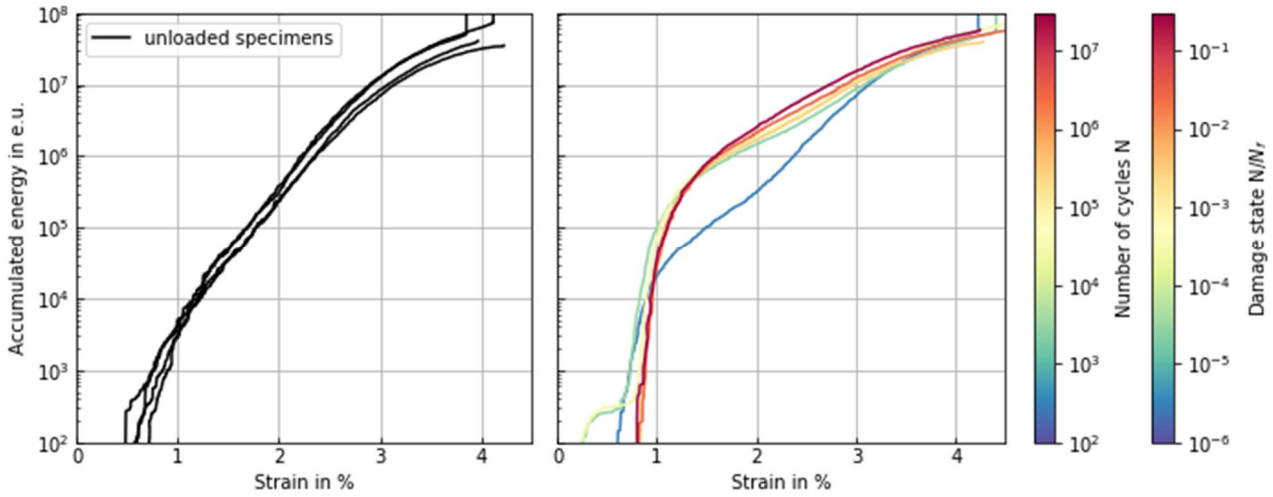

(**a**) (**b**)

Figure 8. Accumulated acoustic energy in energy units (1 e.u. $\hat{=}$ 1×10^{-21} J): (**a**) unloaded specimens; (**b**) preloaded specimens sorted by damage state.

The above observations lead to the conclusion that fatigue loading damage occurs in three stages. For a preloading with 59.9 MPa, these three stages are as follows:

- Stage 1: $N < 10^3$;
- Stage 2: $10^3 \leq N < 10^5$
- Stage 3: $N \geq 10^5$.

In the first stage, only a few damage events are measured at the beginning of the residual strength test. This suggests that fatigue loading with a number of load cycles of less than 10^3 cycles did not cause much damage. The second phase is characterized by the occurrence of isolated acoustic events at a small strain. This indicates that micro-cracks develop between 10^3 and 10^5 cycles, which require low deformation energy to grow further. The AE behavior in the residual strength tests changes again if a preload was applied up to the third stage, indicating that a characteristic damage state is then reached.

3.3. Correlation with S-N Data

Figure 9 shows the S–N test data. The data can be approximated with the logarithmic curve:

$$\sigma_{max} = -9.1 \times \log N + 128.5 \quad (2)$$

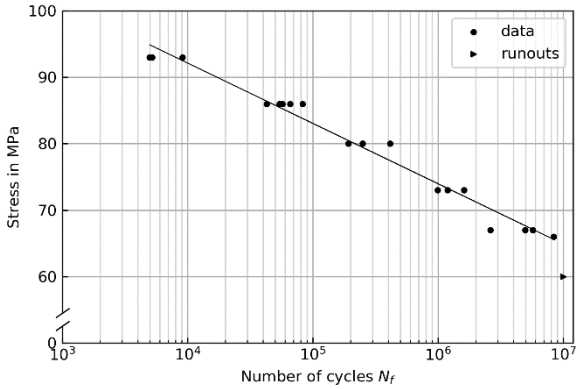

Figure 9. S-N-data.

The test data presented in Figure 6 show that the curves of accumulated acoustic energy in the residual strength tests coincide with those of the unloaded specimens when the maximum stress does not exceed a certain limit value. Therefore, it can be supposed that no damage will be introduced into the material under consideration in the case of cyclic loading with a maximum stress level less than or equal to 26.6 MPa. Equation (1) can be used to extrapolate the average number of load cycles for this maximum stress level to approx. 10^{11}. However, this also means that the endurance limit is reached at the earliest in the range for load cycles greater than 10^{11}, which results in enormous testing times for the experimental verification.

4. Conclusions

Damage initiation under tensile–tensile fatigue loading was studied for short glass fiber reinforced polyamide 6.6. Quasi-static and residual strength tests have been conducted using acoustic emission. The principle of acoustic emission is that each acoustic hit that occurs within the measurement length is associated with a specific damage event. Thus, the evaluation of the recorded acoustic energy allows drawing conclusions about the state of damage. The presented study shows that the analysis of the accumulated acoustic energy is suitable for this purpose.

Comparing the unloaded and preloaded specimens, it was deduced that cyclic loads with a maximum stress of more than 26.6 MPa cause damage in the material. In other words, a so-called fatigue limit or horizontal flattening of the SN curve cannot be expected for a cycle number of up to 10^{11}. This high number of load cycles needed to detect a limit for damage initiation cannot be achieved with the common test methods for fatigue testing. The presented method using acoustic emission shows great potential for the efficient estimation of an endurance or fatigue limit.

In the residual strength test, the acoustic hits and thus the damage events start at a stress and strain level superior to those applied under cyclic preloading. Therefore, it can be concluded that during constant deformation, cyclic loading causes more damage than quasi-static loading. This observation is important for the analysis of material behavior under cyclic loading using quasi-static simulations.

The acoustic behavior in the residual strength tests of the specimens preloaded with the same upper stress level but with a different number of cycles suggests that the damage of short glass fiber-reinforced polyamide 6.6 under fatigue loading occurs in three stages. In the first stage of up to 10^3 load cycles, only a few micro-cracks occur. These micro-cracks form matrix cracks in the second stage of 10^3 and 10^5 load cycles. This process is completed in the third phase from 10^5 load cycles onwards, and is here referred to as the characteristic damage state.

Author Contributions: Conceptualization, methodology, investigation; writing—original draft preparation, J.K.; resources, writing—review and editing, supervision, funding acquisition J.H. Both authors have read and agreed to the published version of the manuscript.

Funding: This research was funded by DFG-GERMAN RESEARCH FOUNDATION, grant number 398483802.

Data Availability Statement: Data are contained within the article.

Acknowledgments: The authors acknowledge the material provided by Lehmann&Voss&Co.

Conflicts of Interest: The authors declare no conflict of interest.

References

1. Mortazavian, S.; Fatemi, A. Effects of fiber orientation and anisotropy on tensile strength and elastic modulus of short fiber reinforced polymer composites. *Compos. Part B Eng.* **2015**, *72*, 116–129. [CrossRef]
2. Wilmes, A.; Hornberger, K. Influence of Fiber Orientation and Multiaxiality on the Fatigue Strength of Unnotched Specimens—Lifetime Estimation. *Procedia Eng.* **2015**, *133*, 148–160. [CrossRef]
3. Doghri, I.; Tinel, L. Micromechanical modeling and computation of elasto-plastic materials reinforced with distributed-orientation fibers. *Int. J. Plast.* **2005**, *21*, 1919–1940. [CrossRef]
4. Launay, A.; Marco, Y.; Maitournam, M.H.; Raoul, I. Constitutive behavior of injection molded short glass fiber reinforced thermoplastics: A phenomenological approach. *Procedia Eng.* **2011**, *10*, 2003–2008. [CrossRef]
5. Kammoun, S.; Doghri, I.; Brassart, L.; Delannay, L. Micromechanical modeling of the progressive failure in short glass–fiber reinforced thermoplastics—First Pseudo-Grain Damage model. *Compos. Part A Appl. Sci. Manuf.* **2015**, *73*, 166–175. [CrossRef]
6. de Monte, M.; Moosbrugger, E.; Quaresimin, M. Influence of temperature and thickness on the off-axis behaviour of short glass fibre reinforced polyamide 6.6—Quasi-static loading. *Compos. Part A Appl. Sci. Manuf.* **2010**, *41*, 859–871. [CrossRef]
7. Bernasconi, A.; Cosmi, F.; Taylor, D. Analysis of the fatigue properties of different specimens of a 10% by weight short glass fibre reinforced polyamide 6.6. *Polym. Test.* **2014**, *40*, 149–155. [CrossRef]
8. Fatemi, A.; Mortazavian, S.; Khosrovaneh, A. Fatigue Behavior and Predictive Modeling of Short Fiber Thermoplastic Composites. *Procedia Eng.* **2015**, *133*, 5–20. [CrossRef]
9. Brunbauer, J.; Mösenbacher, A.; Guster, C.; Pinter, G. Fundamental influences on quasistatic and cyclic material behavior of short glass fiber reinforced polyamide illustrated on microscopic scale. *J. Appl. Polym. Sci.* **2014**, *131*, 40842. [CrossRef]
10. Launay, A.; Marco, Y.; Maitournam, M.H.; Raoult, I. Modelling the influence of temperature and relative humidity on the time-dependent mechanical behaviour of a short glass fibre reinforced polyamide. *Mech. Mater.* **2013**, *56*, 1–10. [CrossRef]
11. ISO. *ISO 13003: Fibre-Reinforced Plastics—Determination of Fatigue Properties under Cyclic Loading Conditions*; ISO: Geneva, Switzerland, 2019.
12. Giordano, M.; Calabro, A.; Esposito, C.; D'Amore, A.; Nicolais, L. An acoustic-emission characterization of the failure modes in polymer-composite materials. *Compos. Sci. Technol.* **1998**, *58*, 1923–1928. [CrossRef]
13. Bohse, J. Acoustic emission characteristics of micro-failure processes in polymer blends and composites. *Compos. Sci. Technol.* **2000**, *60*, 1213–1226. [CrossRef]
14. Huguet, S.; Godin, N.; Gaertner, R.; Salmon, L.; Villard, D. Use of acoustic emission to identify damage modes in glass fibre reinforced polyester. *Compos. Sci. Technol.* **2002**, *62*, 1433–1444. [CrossRef]
15. Karahan, M.; Lomov, S.V.; Bogdanovich, A.E.; Verpoest, I. Fatigue tensile behavior of carbon/epoxy composite reinforced with non-crimp 3D orthogonal woven fabric. *Compos. Sci. Technol.* **2011**, *71*, 1961–1972. [CrossRef]
16. Kempf, M.; Skrabala, O.; Altstädt, V. Acoustic emission analysis for characterisation of damage mechanisms in fibre reinforced thermosetting polyurethane and epoxy. *Compos. Part B Eng.* **2014**, *56*, 477–483. [CrossRef]
17. Carvelli, V.; D'Ettorre, A.; Lomov, S.V. Acoustic emission and damage mode correlation in textile reinforced PPS composites. *Compos. Struct.* **2017**, *163*, 399–409. [CrossRef]
18. Kelkel, B.; Argus, P.; Gurka, M. Scalable Monitoring System for the Localization of Damaging Events in Thin-Walled CFRP Structures Based on Acoustic Emission Analysis and Neural Networks. *Key Eng. Mater.* **2019**, *809*, 401–406. [CrossRef]
19. Sause, M.G.R. *In Situ Monitoring of Fiber-Reinforced Composites: Theory, Basic Concepts, Methods, and Applications*; Springer: Cham, Switzerland, 2016; ISBN 978-3-319-30953-8.
20. Sato, N.; Kurauchi, T.; Sato, S.; Kamigaito, O. Mechanism of fracture of short glass fibre-reinforced polyamide thermoplastic. *J. Mater. Sci.* **1984**, *19*, 1145–1152. [CrossRef]
21. Schoßig, M.; Zankel, A.; Bierögel, C.; Pölt, P.; Grellmann, W. ESEM investigations for assessment of damage kinetics of short glass fibre reinforced thermoplastics—Results of in situ tensile tests coupled with acoustic emission analysis. *Compos. Sci. Technol.* **2011**, *71*, 257–265. [CrossRef]
22. Benz, J.; Willems, F.; Bonten, C. The Sound of Materials. *Kunstst. Int.* **2016**, *11*, 46–49.
23. Bauer, C.; Rief, T.; Hausmann, J.; Schalk, T. A Comparative Study of the Static and Cyclic Acoustic Emission Behavior of Fiber Reinforced Thermoplastics. In Proceedings of the 17th European Conference on Composite Materials (ECCM17), München, Germany, 26–30 June 2016.
24. Jüngert, A.; Dugan, S.; Udoh, A. Acoustic Emission Testing under Difficult Conditions. In Proceedings of the 32nd European Conference on Acoustic Emission Testing, Prague, Czech Republic, 7–9 September 2016.
25. Williams, R.S.; Reifsnider, K.L. Investigation of acoustic emission during fatigue loading of composite specimens. *J. Compos. Mater.* **1974**, *8*, 340–355. [CrossRef]

26. Schorer, N.; Sause, M. *Characterization of CFRP Laminates under Tension-Tension Fatigue Using 3D Digital Image Correlation*; Universität Augsburg: Augsburg, Germany, 2018.
27. Bauer, C. Charakterisierung und Numerische Beschreibung des Nichtlinearen Werkstoff-und Lebensdauerverhaltens eines Kurzglasfaserverstärkten Polymerwerkstoffes unter Berücksichtigung der im μCT gemessenen Lokalen Faserorientierung. Ph.D. Thesis, TU Kaiserslautern, Kaiserslautern, Germany, 2017.
28. DIN Deutsches Institut für Normung e.V. *DIN EN ISO 527-1: Kunststoffe-Bestimmung der Zugeigenschaften-Teil 1: Allgemeine Grundsätze*; DIN: Berlin, Germany, 2019.
29. Akaike, H. Markovian representation of stochastic processes and its application to the analysis of autoregressive moving average processes. In *Selected Papers of Hirotugu Akaike*; Springer: Berlin, Germany, 1998; pp. 223–247.